

# A Multi-Channel Algorithm for Edge Detection Under Varying Lighting Conditions

Wei Xu

University of Colorado at Boulder  
Department of Computer Science  
Boulder, CO 80309-0430 USA

Wei.Xu@colorado.edu

Michael Jenkin, Yves Lespérance

York University

Department of Computer Science and Engineering  
4700 Keele St., Toronto, ON M3J 1P3 CANADA

{jenkin, lesperan}@cs.yorku.ca

## Abstract

*In vision-based autonomous spacecraft docking multiple views of scene structure captured with the same camera and scene geometry is available under different lighting conditions. These “multiple-exposure” images must be processed to localize visual features to compute the pose of the target object. This paper describes a robust multi-channel edge detection algorithm that localizes the structure of the target object from the local gradient distribution computed over these multiple-exposure images. This approach reduces the effect of the illumination variation including the effect of shadow edges over the use of a single image. Experiments demonstrate that this approach has a lower false detection rate than the average response of the Canny edge detector applied to the individual images separately.*

## 1. Introduction

In the process of vision-based autonomous spacecraft docking, an essential issue is to accurately estimate the relative position and orientation (the pose) of the docking target based on images taken by the chaser vehicle. Multiple images can be captured in each sampling period to provide adequate edge information of the structure of the docking target [4]. These “multiple-exposure” images, which can be taken to have the same capture geometry (considering the low relative speed between the chaser and the target during a sampling period) are captured under different illumination conditions. The resulting image set can be viewed as a multi-channel image. Figure 1(a) illustrates the docking task as the chaser approaches the target. Successful docking requires an accurate estimate of the pose of the target relative to the chaser. The target may be equipped with a special purpose docking fixture that includes a visual docking target as shown in Figure 1(b), but this is not always the case. In either case, controllable illumination and a fixed

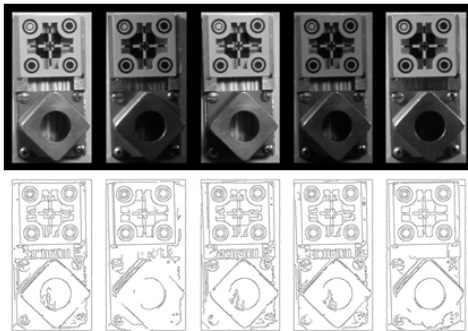
but adjustable camera are used to obtain multiple-exposure images of the target. The underlying computation problem then becomes one of extracting image features from the set of multiple-exposure images so as to establish the target’s pose relative to the chaser.

Given the multiple-exposure image set, how should image features be extracted in order to localize the docking target? Here we describe a novel multi-channel edge detection algorithm to solve the edge detection problem for multiple-exposure images. The goal of the multi-channel edge detection algorithm is to seek edges corresponding to the physical structure of real objects (e.g., the docking target) from the multiple-exposure images and in the process to identify and reduce the influence of edges that arise only due to illumination changes (i.e. shadow edges) and other random noise. These noise edge signals can disturb the observation of the edge structure and degrade the estimation of the pose of the docking target.

It is significantly more difficult to analyze edges in multi-channel images than in a single image because different channels may contain only partial or conflicting edge information about the structure of the target. When the conflict is slight, simple logical or mathematical operations (e.g., logical OR operation, majority voting, arithmetic average) can be applied to merge the multiple channels into a single output. This is a widely used approach in multi-spectral edge detection [3, 7, 15], color edge detection [12], and multi-flash edge detection [13]. When the conflict is more pronounced, a more sophisticated merging approach is required. Here, we distinguish between the edge structure and noise edge signals by their gradient distributions. Under a range of illumination conditions, the former should be more stable than the latter in a statistical sense. Observation and experimental verification [14] show that the local gradient orientations in multiple-exposure images around an edge can be well described by a Gaussian distribution centered at the orientation of the underlying edge corrupted



(a) Spacecraft docking

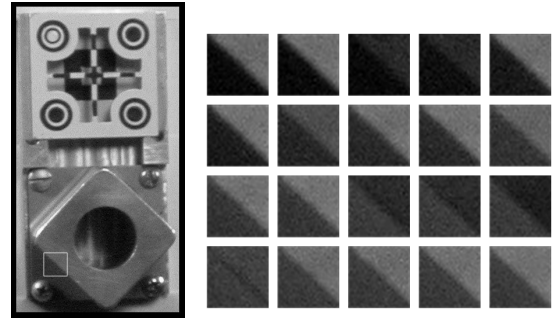


(b) Multiple-exposure images of the docking target

Figure 1. Spacecraft docking. (a) shows a simulation of the overall task. Image courtesy of MDA Space Missions. (b) shows multiple-exposure images of a mockup of a docking target (a grapple fixture) and their individual edge maps. For each image, the corresponding Canny edge map ( $\sigma = 1.0$ ) is shown directly below the image.

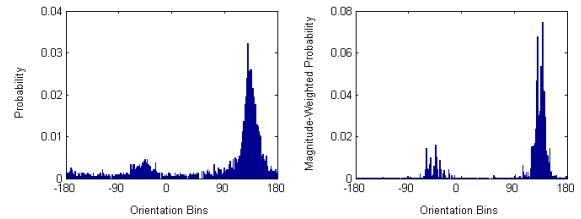
by outlying gradient orientation samples (Figure 2). Figure 2(a) shows a single image of the mockup of a grapple fixture including its visual target. A small test window area is identified on the bottom-left side of the image. Figure 2(b) shows 20 views of this test area obtained under different illumination and camera capture settings. A sampling square window was centered on this test region within which pixel gradient samples were collected from multiple channels and grouped together for statistical analysis. Figures 2(c) shows the probability distribution and weighted probability distributions of the collected multi-channel gradient data. The prime gradient orientation near 135 degrees is corrupted by small but significant outliers. These outlying gradients can corrupt the local gradient estimation (see Figure 2(d)) even though they may occupy only a small fraction of the entire gradient sample. The problem is to identify and remove the outliers while merging the inlying gradient samples.

A common approach to dealing with this type of robust estimation process (see [11, 1, 8, 10] for applications in computer vision) is to model the corrupted dataset using a

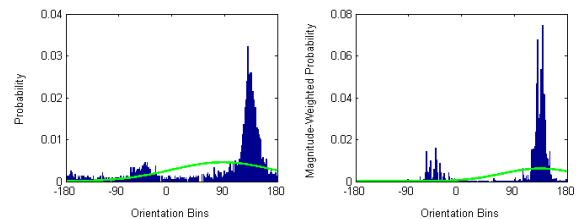


(a) The test area (the white rectangle)

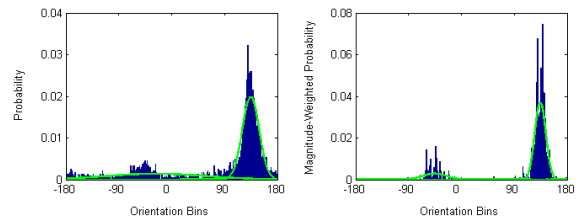
(b) Sample clips over a step edge



(c) Probability distribution and magnitude weighted probability distribution within the sampling window centering in the test region (window size: 11x11 pixels).



(d) Non-robust estimation: the entire data are modelled by a single distribution. No special treatment for the outliers. Non-weighted and magnitude weighted probability distributions are shown.



(e) Robust estimation: the inliers and outliers are modelled separately and the estimation is computed from the inlier (main) distribution only. Non-weighted and weighted probability distributions are shown.

Figure 2. The use of non-robust and robust approaches to estimate the probability distributions around an inherent step edge but affected by varying lighting conditions. (b) shows a set of 20 channels of the same test area (marked out by a white rectangle in (a)) centered at an object edge (window size: 40x40 pixels). (c) shows the gradient distribution within a sampling window around the center of the clips. (d) and (e) show the results obtained using non-robust and robust estimations.

two-component mixture model in which the inliers and the

outliers are separately modelled by a simple distribution, e.g. the Gaussian distribution (see Figure 2(e)). We utilize this decomposition approach here within a multi-channel edge detection process to separate gradient information associated with edge structure from unstable shadow edges and other noise in the image.

## 2. The approach

Our approach is to extend the single-channel Canny edge detector [6] to operate on multiple channels (see Figure 3). Input images are first processed in separate processing channels (one image per channel) to obtain individual gradient maps. Following the single-channel Canny algorithm, the effect of additive high frequency noise in an input image  $\vec{I}$  is attenuated by convolving the image with a low-pass two-dimensional symmetric Gaussian filter  $\vec{G}_{\sigma,\sigma}$ . The width of the Gaussian filter  $\sigma$  is a user-defined parameter that determines the degree of smoothing and the cut-off frequency. Let  $\vec{I}' = \vec{G}_{\sigma,\sigma} * \vec{I}$  represent the result of this computation. The gradients along the x-axis and y-axis directions of the smoothed image  $\vec{I}'$  are computed as:  $D_x = \frac{\partial}{\partial x}[G_x * \vec{I}'] = \frac{\partial G_x}{\partial x} * \vec{I}'$  and  $D_y = \frac{\partial}{\partial y}[G_y * \vec{I}'] = \frac{\partial G_y}{\partial y} * \vec{I}'$  where  $G_x$  and  $G_y$  are one-dimensional Gaussian filters in x-axis and y-axis directions. The magnitude  $w$  and local orientation  $\phi$  of the gradient are computed as  $w^2 = D_x^2 + D_y^2$  and  $\phi = \tan^{-1} D_y/D_x$ . These computations are performed separately for each channel and at each pixel position.

The next stage is to combine the local edge support using a robust statistical scheme operating within a small sampling window for each pixel in the image  $\vec{I}$ . At each pixel position  $(x, y)$ , the local gradient orientation distribution within the window is modelled as a two-component Gaussian Mixture Model (GMM) [2] in which the inliers (the normal gradient samples corresponding to the local edge structure) are modelled by the main Gaussian distribution and the outliers (gradients corresponding to shadow edges and other random noise) are modelled by a background Gaussian distribution. The Expectation Maximization (EM) algorithm [2] is used to decompose the mixture model, and to identify and separate the outliers from the inliers.

The gradient data from the channels are binned based on their orientation so that the gradient orientation probability distribution can be inferred from the bin frequencies. Suppose we have collected  $N$  gradient samples ( $N = W * W * n_c$  where  $W$  is the width of the square sampling window and  $n_c$  is the number of channels) and represent sample  $j$  as  $(\phi_j, w_j)$  where  $\phi_j$  and  $w_j$  are the orientation and magnitude of sample  $j$  respectively. Let the total number of orientation bins be  $K$  and represent bin  $i$  as  $(\theta_i, M_i)$  where  $\theta_i$  and  $M_i$  are the center orientation and magnitude of bin  $i$  respectively.  $sample_j \in bin_i \Leftrightarrow \theta_i - W_\theta/2 < \phi_j \leq \theta_i + W_\theta/2$  where  $W_\theta$  is the width of the bin. We define  $M_i$  as the sum

of magnitudes of the samples falling into the same bin  $i$ , i.e.

$$M_i = \sum_{sample_j \in bin_i} w_j.$$

Given  $m_{ij}$  the membership function of sample  $j$  with respect to bin  $i$  (i.e.  $m_{ij} = 1$  if  $sample_j \in bin_i$ ; otherwise  $m_{ij} = 0$ ), the magnitude-weighted frequency of any bin  $i$  can be written as  $f_i = M_i = \sum_{j=1}^N w_j m_{ij}$ . Magnitude-weighted frequencies are used instead of normal frequencies in our analysis of the gradient orientation distribution. This is based on the intuition that a gradient sample with a larger magnitude provides stronger evidence of the edge's true orientation than a gradient sample with a smaller magnitude. Note that the gradient orientation bins of shadow edges are weighted less than those of object edges since shadow edges are less stable and normally have fewer samples (channels) falling into the same bin. This operation enlarges the differences between the distributions of these two kinds of gradients and makes it easier to distinguish between them.

The EM algorithm is used to estimate the most-likely gradient value at the pixel position  $(x, y)$  using the weighted frequencies. The two-component GMM for this pixel position is given by [2]:

$$f(\theta) = \sum_{m=1}^2 \alpha_m p_m(\theta | \mu_m, \sigma_m) \quad (1)$$

where  $\alpha_m$  and  $p_m$  are the mixing coefficient and probability distribution function of the  $m$ 'th component Gaussian distribution.  $p_m$  is assumed to be a Gaussian:

$$p_m(\theta | \mu_m, \sigma_m) = \frac{1}{\sqrt{2\pi}\sigma_m} e^{-\frac{d^2}{2\sigma_m^2}} \quad (2)$$

where  $\mu_m$  and  $\sigma_m$  are the mean and standard deviation of the  $m$ 'th distribution. These two parameters and the mixing coefficient  $\alpha_m$  are estimated by the EM algorithm. Note that because  $\theta$  (in degrees) represents the gradient orientation which is an angular variable, the circular distance  $d = \min(|\theta - \mu_m|, 360 - |\theta - \mu_m|)$  is used instead of the normal distance  $|\theta - \mu_m|$  in equation (2).

The estimation of the parameters in the mixture model is refined in iterations following the EM algorithm update functions:

$$p_i(m | \theta_i, \Theta^{(t)}) = \frac{\alpha_m^{(t)} p_m(\theta_i | \mu_m^{(t)}, \sigma_m^{(t)})}{\sum_{l=1}^2 \alpha_l^{(t)} p_l(\theta_i | \mu_l^{(t)}, \sigma_l^{(t)})} \quad (3)$$

$$\alpha_m^{(t+1)} = \sum_{i=1}^K \frac{f_i}{\sum_{l=1}^K f_l} \cdot p_i(m | \theta_i, \Theta^{(t)}) \quad (4)$$

$$\mu_m^{(t+1)} = \frac{180}{\pi} \cdot \frac{\sum_{i=1}^K f_i p_i(m | \theta_i, \Theta^{(t)}) \cos \theta_i}{\sum_{i=1}^K f_i p_i(m | \theta_i, \Theta^{(t)}) \sin \theta_i} \quad (5)$$

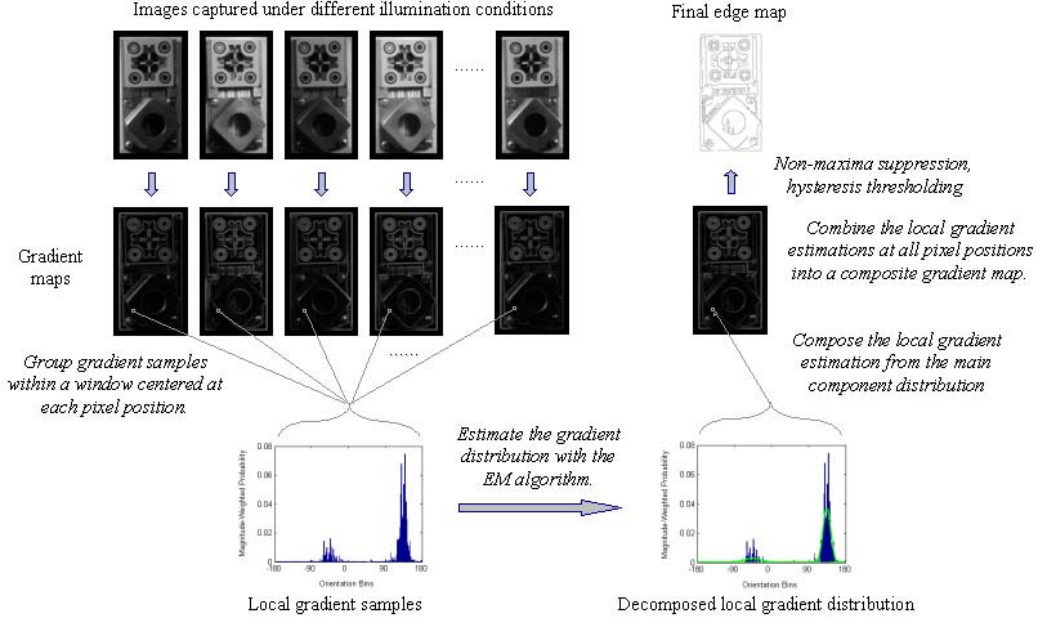


Figure 3. Outline of the multi-channel edge detection algorithm.

$$\sigma_m^{(t+1)} = \frac{\sum_{i=1}^K f_i p_i(m | \theta_i, \Theta^{(t)}) d_{im}^2}{\sum_{i=1}^K f_i p_i(m | \theta_i, \Theta^{(t)})} \quad (6)$$

where  $m \in \{1, 2\}$  whose value represents the  $m$ 'th component distribution;  $K$  is the number of gradient orientation bins and  $\theta_i$  and  $f_i$  are the central orientation and magnitude-weighted frequency of bin  $i$ ;  $\Theta^{(t)} = \{\alpha_m^{(t)}, \mu_m^{(t)}, \sigma_m^{(t)}\}$  is the estimated parameter set at iteration  $t$  and  $\alpha_m^{(t)}$ ,  $\mu_m^{(t)}$  and  $\sigma_m^{(t)}$  are the mixing coefficient, mean and standard deviation of the  $m$ 'th component distribution;  $d_{im}$  is the circular distance from  $\theta_i$  to  $\mu_m^{(t)}$ . The magnitude weighted frequencies  $f_i$  are used as weights in the computation of  $\Theta^{(t)}$ .

The (non-robust) weighted mean and standard deviation of the gradient bins are used to initialize the EM algorithm (with distribution 1 set at the location of the non-robust mean and distribution 2 set 180 degrees away from distribution 1). After the EM algorithm terminates, the gradient of the local edge structure is estimated from the distribution of the inliers. Suppose  $\alpha_1 > \alpha_2$ , then the estimated gradient orientation is the mean of the main Gaussian distribution  $\mu_1$ . The corresponding magnitude is composed as  $\alpha_1 \sum_{i=1}^K M_i$ , which represents the proportion of all the sample magnitudes that are generated by the main distribution.

The result of the EM process is a composite gradient  $(\mu_1, \alpha_1 \sum_{i=1}^K M_i)$  for each pixel position. A composite gradient map corresponding to the underlying edge structure is then computed by combining the local gradient estimates at all of the pixel positions. Based on this composite

gradient map an edge map is finally obtained using the post-processing techniques of the Canny edge detector [6].

### 3. Experimental evaluation

We have evaluated our algorithm using images of both simple structured objects and mockups of space hardware. As with any complex algorithm, a group of parameters must be specified:

- $\sigma$  - the width of the Gaussian smoothing filter [6];
- $\tau_h$  - the higher threshold on the gradient magnitudes for hysteresis thresholding [6];
- $\tau_l$  - the lower threshold on the gradient magnitudes for hysteresis thresholding [6];
- $n_c$  - the number of channels, i.e. the size of the image set;
- $W$  - the width of the local sampling window (assuming a square window is used);
- $W_\theta$  - the width of the orientation bins;
- $t_{max}$  - the maximum number of iterations (i.e. convergence threshold) in the EM algorithm [2];
- $\tau_L$  - the threshold on the increment of the log-likelihood in the EM algorithm [2].

$\sigma$ ,  $\tau_h$  and  $\tau_l$  are parameters of the Canny edge detector.

In our experiments, multi-channel edge detection results were evaluated with images pre-processed with the same  $\sigma$  values in order to avoid differences introduced by different smoothing levels. However,  $\tau_h$  and  $\tau_l$  varied for individual images in order to obtain optimal single-channel edge maps (optimal by inspection).  $n_c$ ,  $W$  and  $W_\theta$  are the spe-

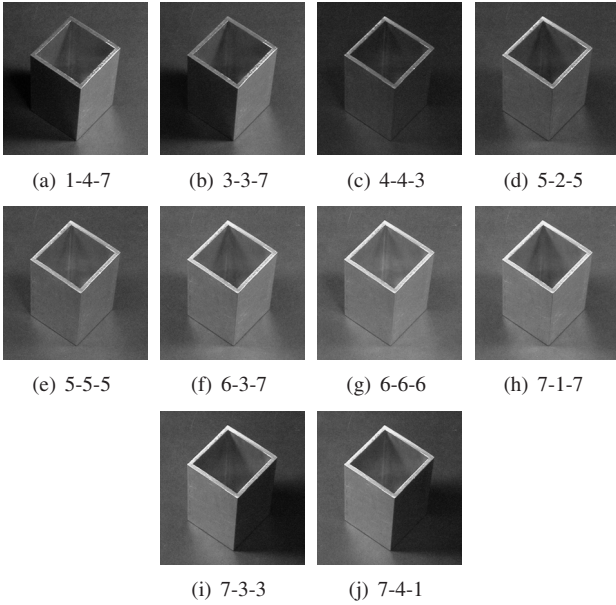


Figure 4. A set of ten multiple-exposure images of an experimental cube. The numbers under an image indicates the intensity levels of lights from the upper-left, upper-middle and upper-right directions. The higher a number the stronger the light intensity.

cific parameters of the multi-channel algorithm.  $n_c$  varied as different image sets were used, while  $W = 1$  (i.e. pixel-wise) and  $W_\theta = 1$  for the experiments demonstrated here.  $t_{max}$  and  $\tau_L$  affect the termination of the EM algorithm. They were set to 30 and  $10^{-6}$  respectively based on prior experience (see [14] for details).

Simple structured objects are especially useful for quantitative evaluations because their ground-truth edge maps can be measured relatively easily. A set of ten multiple-exposure images ( $n_c = 10$ ) of an experimental cube is given in Figure 4. Figure 5 shows the results of applying the single-channel Canny edge detector to each of the images and of applying the multi-channel edge detection algorithm to the entire image set. Table 1 and Table 2 list the false positive detection rate (FPR) and false negative detection rate (FNR) of edgels in the edge maps shown in Figure 5.  $\tau_d$  is a pre-defined distance threshold for judging whether a detection is correct: Only when the distance from a detected edgel  $e$  to the closest model edge  $d(e)$  is below  $\tau_d$ , is edgel  $e$  regarded as a correct detection.

Table 1 shows that the multi-channel algorithm always has a lower FPR than the single-channel Canny edge detector. This means that the multi-channel algorithm is more robust to illumination changes and thus its edge map contains fewer relatively unstable edges that lead to misdetections. Table 2 shows that although the Canny edge detector occasionally has a lower FNR than the multi-channel algorithm for certain illumination conditions, the multi-channel algorithm consistently outperforms the average response of the

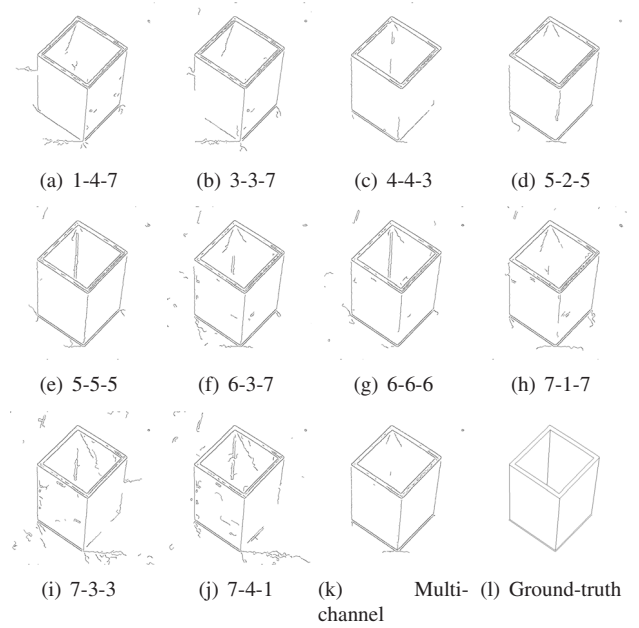


Figure 5. The edge maps computed using the single-channel Canny edge detector, the edge map generated by the multi-channel edge detection algorithm and the hand measured ground truth edge map ( $\sigma = 2.0$ ).

	$\tau_d = 0.5$	$\tau_d = 1.0$	$\tau_d = 2.0$
(a) 1-4-7	0.7163	0.5168	0.3610
(b) 3-3-7	0.7008	0.5065	0.3714
(c) 4-4-3	0.6437	0.3978	0.2333
(d) 5-2-5	0.6626	0.4396	0.2918
(e) 5-5-5	0.6639	0.4517	0.3129
(f) 6-3-7	0.6871	0.4975	0.3718
(g) 6-6-6	0.6579	0.4434	0.3154
(h) 7-1-7	0.6662	0.4756	0.3655
(i) 7-3-3	0.7391	0.5688	0.4505
(j) 7-4-1	0.7615	0.5898	0.4578
average	0.6899	0.4886	0.3531
multi-channel	0.5825	0.3354	0.1753

Table 1. False positive detection rates (FPR's) of the cube images with different distance thresholds ( $\tau_d$ 's, in pixels).

Canny edge detector over the entire range of the provided illumination conditions.

Figure 7 illustrates the ability of the multi-channel algorithm to reduce the effect of shadow edges on a mockup of a docking fixture. A set of 20 multiple-exposure images ( $n_c = 20$ ) of the mockup of the docking fixture were used (see Figure 6). The edge map generated by the multi-channel algorithm was computed with  $n_c = 20$ ,  $W = 1$ ,  $\sigma = 1.0$ ,  $\tau_h = 20$  and  $\tau_l = 10$ . Note that in the image "2-7-5" (Figure 7(a)) the area near the bottom-left corner is covered by shadows cast from the upper-right. The under-

	$\tau_d = 0.5$	$\tau_d = 1.0$	$\tau_d = 2.0$
(a) 1-4-7	0.4738	0.2575	0.1655
(b) 3-3-7	0.4774	0.2827	0.2167
(c) 4-4-3	0.5142	0.3551	0.2715
(d) 5-2-5	0.4494	0.2899	0.1831
(e) 5-5-5	0.3862	0.2091	0.1032
(f) 6-3-7	0.4114	0.2671	0.1283
(g) 6-6-6	0.3790	0.2035	0.1116
(h) 7-1-7	0.4062	0.2859	0.1735
(i) 7-3-3	0.4698	0.3099	0.1691
(j) 7-4-1	0.5086	0.3095	0.1731
average	0.4476	0.2770	0.1696
multi-channel	0.3758	0.2079	0.1096

Table 2. False negative detection rates (FNR's) of the cube images with different distance thresholds ( $\tau_d$ 's, in pixels).

lying edge structure should be straight and nearly vertical in this region, but some edges are seriously distorted by the shadows (see the same location in the corresponding edge map). This distortion is rectified in the edge map generated by the multi-channel algorithm (Figure 7(c)). The multi-channel algorithm also removed the shadow edges over the area a little below the top-right corner of the image "7-3-3" (Figure 7(b)).

Based also on the grappling fixture image set, Figure 8 provides a comparison between the logical combinations of the individual edge maps computed by the Canny edge detector and the edge map computed by the multi-channel algorithm directly. The left three images are the combined edge maps obtained by merging all of the individual edge maps using simple logical operations (AND, OR and majority-voting). The logical AND and OR operations are very vulnerable to illumination changes. There is almost no edge structure in the combined edge map using the AND operation, while the results of using the OR operation are extremely fuzzy. The majority-voting scheme [9] is more robust and works better than either the AND or the OR operation, but its mechanism of distinguishing outliers is susceptible to failure. Many edges are disconnected (especially the long edges) and even disappear in the combined edge map. These problems do not exist in the edge map computed by the multi-channel algorithm (the right-most image).

If all space targets were pre-positioned, then special purpose target tracking software could be developed to track exactly those targets. (And the targets themselves would be specially designed in order to simplify the task.) Indeed this is the case for the docking latch target, which was specifically designed to permit algorithms to compute the relative pose of the target. Unfortunately not all targets fall into this category. Figure 9 shows a set of 20 multiple-exposure images of a mockup of a latch from the Hubble Space Tele-

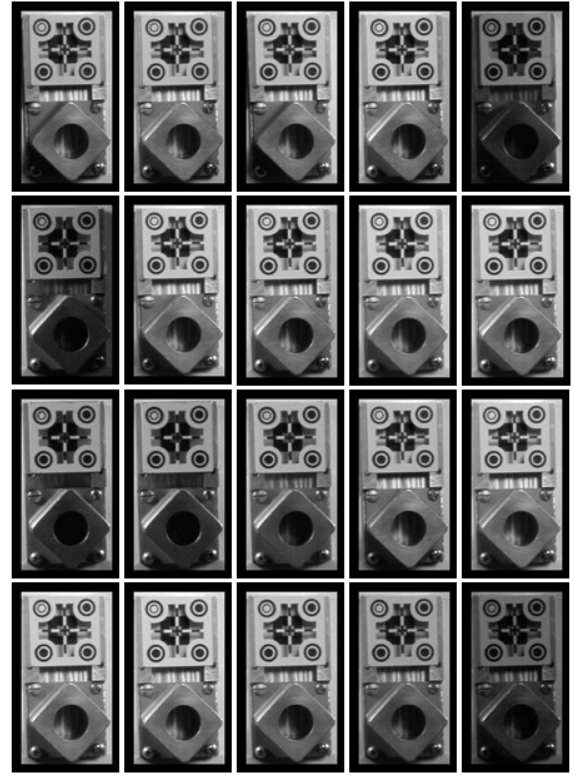


Figure 6. Image set of the mockup of the grappling fixture. The original image size is 336x584 pixels.

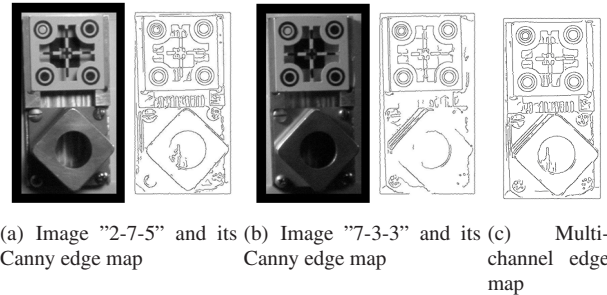


Figure 7. Comparison between single edge maps and the multi-channel edge map ( $\sigma = 1.0$ ).

scope. On-orbit servicing of the Hubble Space Telescope requires accurate docking with these latches. The latches are not painted in a manner to simplify this task, and the latch itself has a complex 3D structure.

Considering the high level of image noise present in the latch images, the performance of the multi-channel approach was evaluated at different noise suppression levels (i.e. with different  $\sigma$  values). Figure 10 and Figure 11 provide a comparison between the logical combinations of the individual edge maps computed by the Canny edge detector and the edge map computed by the multi-channel algorithm with  $\sigma = 1.0$  and  $\sigma = 2.0$  respectively. As in previous ex-

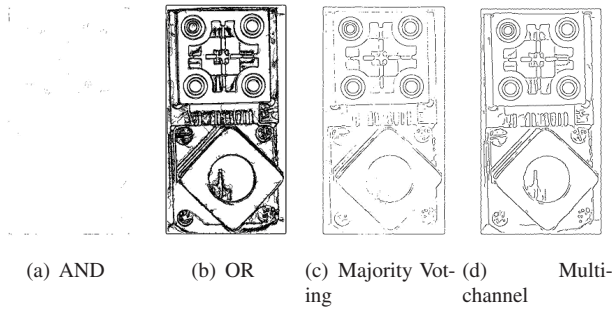


Figure 8. Logical combinations of individual edge maps of the grappling fixture and the edge map computed by the multi-channel approach.

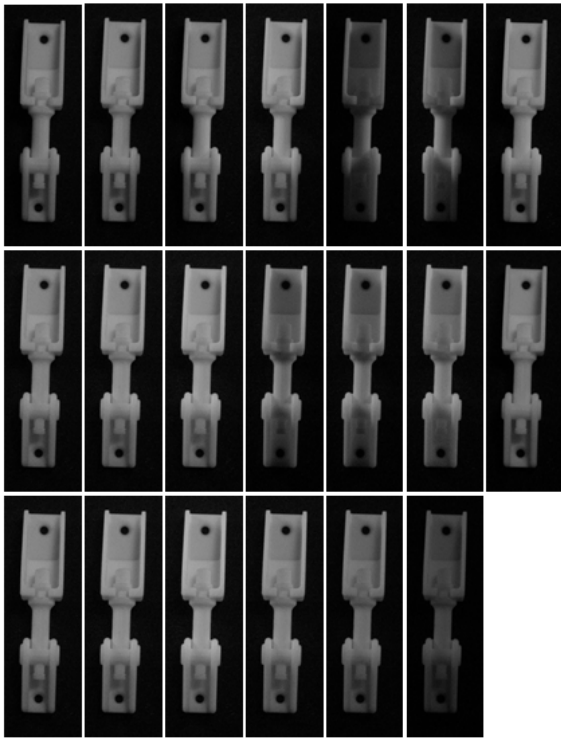


Figure 9. Image set of the mockup of the Hubble Space Telescope latch. The original image size is 300x920 pixels.

amples, the left three images show the logical combinations of the individual edge maps, and the rightmost map shows the edge map obtained using the multi-channel algorithm. With the noise suppression level increased from  $\sigma = 1.0$  to  $\sigma = 2.0$ , the performance of both the single-channel Canny edge detector and the multi-channel approach are improved, especially the single-channel Canny edge detector. However, at neither suppression level does the logical combinations of individual Canny edge maps capture the detail obtained with the multi-channel algorithm. The large performance improvement of the single-channel Canny edge

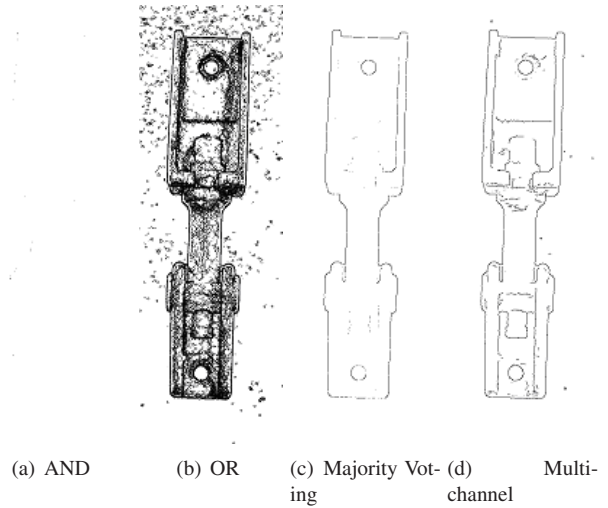


Figure 10. Logical combinations of individual edge maps of the Hubble Space Telescope latch and the edge map computed by the multi-channel approach (with  $n_c = 20$ ,  $W = 1$ ,  $\sigma = 1.0$ ,  $\tau_h = 20$  and  $\tau_l = 15$ ).

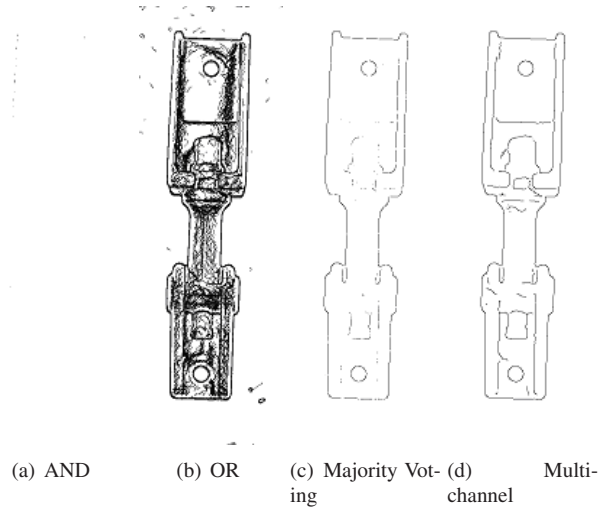


Figure 11. Logical combinations of individual edge maps of the Hubble Space Telescope latch and the edge map computed by the multi-channel approach (with  $n_c = 20$ ,  $W = 1$ ,  $\sigma = 2.0$ ,  $\tau_h = 25$  and  $\tau_l = 5$ ).

detector due to the increase of the noise suppression rate demonstrates its sensitivity to parameter changes. Its robustness to noise depends greatly on correctly setting the parameter corresponding to the noise suppression rate. In contrast, the robustness of the multi-channel approach originates from its internal robust combination and outlier removal scheme.

#### 4. Discussion and Conclusions

The composite gradient map computed by the multi-channel edge detection algorithm that we have proposed re-

tains those parts of the image gradient that are statistically consistent over the illumination changes associated with the input images, and discards unstable parts. An edge map computed from this gradient map better indicates the underlying structure of the scene, since the influence of shadow edges and random noise, which are generally less stable under illumination changes, is reduced. This special characteristic of multi-channel edge detection is crucial to applications that operate under varying illumination conditions, including spacecraft docking, underground mining, underwater mapping, and some medical applications.

Experiments show that for a set of multiple-exposure images that corresponds to a range of illumination conditions, the multi-channel approach outperforms both the average response of the Canny edge detector applied to the individual images separately and the logical combinations of the individual responses. However, as a robust statistical method, the multi-channel approach has its limitations. It requires that the outliers only occupy a small part of the whole gradient samples. It may fail under particular or extreme illumination conditions, e.g. over-exposure and under-exposure, since the number of outliers increases dramatically in such cases.

The proposed multi-channel edge detection algorithm has been used to build a complete prototype pose estimation system [5]. Currently, the algorithm can process an image set composed of six 336x584 pixels size images (of the grappling fixture) in 10 seconds and a set of twenty images of the same size in one minute (both using a pixelwise sampling window), running on a Linux server (Intel Xeon CPU 3.06 GHz x 4, 3.7G memory and Linux 2.4.29 SMP). However, in spacecraft docking very high-resolution images are frequently used (e.g. 2560x1920 pixels). The speed of the algorithm will need to be improved for space deployment. Parallelization and a hardware implementation of the algorithm may be needed.

## 5. Acknowledgement

The research described in this paper is part of the CITO (Communication Information Technology Ontario) "Lights and Camera" project. The authors would like to thank MDA Space Missions for its financial support to this research. The authors would also like to thank Dr. Jane Mulligan for her help in preparing this manuscript.

## References

[1] W. A. Almageed and C. E. Smith. Mixture models for dynamic statistical pressure snakes. In *Proc. IEEE ICPR*, volume 2, pages 721–724, 2002.

[2] J. A. Bilmes. A gentle tutorial of the EM algorithm and its application to parameter estimation for Gaussian Mixture

and Hidden Markov Models. Technical Report ICSI-TR-97-021, University of California at Berkeley, 1997.

[3] P. Bonnin, B. Hoeltzener-Douarin, and E. Pissaloux. A new way of image data fusion: the multi-spectral cooperative segmentation. In *Proc. IEEE ICIP*, volume 3, pages 572–575, 1995.

[4] O. Borzenko, Y. Lespérance and M. Jenkin. Controlling camera and lights for intelligent image acquisition and merging. In *Proc. 2nd Canadian Conf. on Computer and Robot Vision*, pages 602–609, 2005.

[5] O. Borzenko, W. Xu, M. Obsniuk, A. Chopra, P. Jasiobedzki, M. Jenkin and Y. Lespérance. Lights and Camera: Intelligently Controlled Multi-channel Pose Estimation System. In *Proc. of the 4th IEEE Intl. Conf. on Computer Vision Systems (ICVS'06)*, page 42, 2006.

[6] J. F. Canny. A computational approach to edge detection. *IEEE PAMI*, 8:679–698, 1986.

[7] A. Cumani. Edge detection in multispectral images. *CVGIP: Graphical Models and Image Processing*, 53(1):40-51, 1991.

[8] A. Jepson and M. J. Black. Mixture models for optical flow computation. In *Proc. IEEE CVPR*, pages 760-761, 1993.

[9] L. Lam and C. Y. Suen. Application of Majority Voting to Pattern Recognition: An Analysis of its Behaviour and Performance. *IEEE Trans. on Syst. Man and Cybrn. - Part A: Systems and Humans*, 27:553-568, 1997.

[10] P. E. Lopez-de-Teruel and A. Ruiz. A parallel algorithm for Tracking of segments in noisy edge images. In *Proc. IEEE ICPR*, volume 4, pages 807–811, 2000.

[11] N. Ludtke, B. Luo, E. Hancock and R. C. Wilson. Corner detection using a mixture model of edge orientation. In *Proc. IEEE ICPR*, volume 2, pages 574–577, 2002.

[12] F. Porikli. Accurate detection of edge orientation for color and multi-spectral imagery. In *Proc. IEEE ICIP*, volume 1, pages 886–889, 2001.

[13] R. Raskar, K. H. Tan, R. Feris, J. Yu, and M. Turk. Non-photorealistic camera: depth edge detection and stylized rendering using multi-flash imaging. *ACM Trans. on Graphics*, 23(3):679–688, 2004.

[14] W. Xu. Mutli-channel Edge Detection. Master's thesis, York University, Toronto, Canada, 2005.

[15] A. Zia, V. DeBrunner, A. Chinnaswamy, and L. Debrunner. Multi-resolution and multi-sensor data fusion for remote sensing in detecting air pollution. In *Proc. IEEE Southwest Symp. on Image Analysis and Interpretation*, pages 9–13, 2002.